Contrib Mineral Petrol (1991) 107:373–386

Contributions to Mineralogy and Petrology

Petrology and geochemistry of the Huerto Andesite, San Juan volcanic field, Colorado

Daniel R.R. Askren, James A. Whitney, and Michael F. Roden

Department of Geology, University of Georgia, Athens, GA 30602, USA

Received September 27, 1990 / Accepted October 9, 1990

Abstract. The Huerto Andesite is the largest of several andesite sequences interlayered with the large-volume ash-flow tuffs of the San Juan volcanic field, Colorado. Stratigraphically this andesite is between the region's largest tuff (the 27.8 Ma, 3,000 km^3 Fish Canyon Tuff) and the evolved product of the Fish Canyon Tuff (the 27.4 Ma, 1,000 km^3 Carpenter Ridge Tuff), and eruption was from vents located approximately 20–30 km southwest and southeast of calderas associated with these ash-flow tuffs. Olivine phenocrysts are present in the more mafic, SiO_2-poor samples of andesite, hence the parent magma was most likely a mantle-derived basaltic magma. The bulk compositions of the olivine-bearing andesites compared to those containing orthopyroxene phenocrysts suggest the phenocryst assemblage equilibrated at 2–5 kbar. Two-pyroxene geothermometry yields equilibrium temperatures consistent with near-peritectic magmas at 2–5 kbar. Fractionation of phenocryst phases (olivine or orthopyroxene + clinopyroxene + plagioclase + Ti-magnetite + apatite) can explain most major and trace element variations of the andesites, although assimilation of some crustal material may explain abundances of some highly incompatible trace elements (Rb, Ba, Nb, Ta, Zr, Hf) in the most evolved lavas. Despite the great distance of the San Juan volcanic field from the inferred Oligocene destructive margin, the Huerto Andesite is similar to typical plate-margin andesites: both have relatively low abundances of Nb and Ta and similar values for trace-element ratios such as La/Yb and La/Nb.

Deriving the Fish Canyon and Carpenter Ridge Tuffs by crystal fractionation from the Huerto Andesite cannot be dismissed by major-element models, although limited trace-element data indicate the tuffs may not have been derived by such direct evolution. Alternatively, heat of crystallization released as basaltic magmas evolved to andesitic compositions may have caused melting of crust to produce the felsic-ash flows. Mafic magmas may have been gravitationally trapped below lighter felsic magmas; mafic magmas which ascended to the surface probably migrated upwards around the margins of silicic chambers, as suggested by the present-day outcrops of andesitic units around the margins of recognized ash-flow calderas.

Offprint requests to: D.R.R. Askren

Introduction

The San Juan volcanic field of south-central Colorado covers approximately 25,000 km^2 (Steven and Lipman 1976) and erupted contemporaneously with other voluminous Oligocene-Early Miocene volcanic centers in the western United States (Indian Peak caldera complex, Utah-Nev; Central Nevada volcanic center, Nev; Mogollon-Datil volcanic field, N.M.; Marysvale volcanic field, Utah; Sierra Madre Occidental volcanic field, western Mexico). Volcanism in the San Juan volcanic field began about 35–30 Ma with the Conejos Formation – a volcanic sequence dominated by andesite, with lesser amounts of dacite, and minor rhyolite (Lipman 1975; Zielinski and Lipman 1976; Colucci et al. 1988). About 30 Ma activity began changing to eruptions of thousands of cubic kilometers of dacitic and rhyolitic ash-flow tuffs, with minor amounts of andesite (Lipman 1975). About 26 Ma the character of volcanism changed again to bimodal basalt and rhyolite eruptions (Hinsdale Formation).

The Huerto Andesite (Lipman 1975, p. 55) is stratigraphically bound by the 3,000 km^3, 27.8 Ma Fish Canyon Tuff and the 1,000 km^3, 27.6 Ma Carpenter Ridge Tuff (Lanphere 1988) and erupted from volcanic centers in the South Fork (Lipman and Steven 1976; Askren 1986) and Squaw Mesa areas (Fig. 1). Previously, Larsen and Cross (1956, p. 143) used the name "Huerto quartz latite" (defining it as "dark quartz latites" that lie between two felsic units that have been subsequently remapped). Steven and Ratté (1965, p. 32) used the name "Huerto Formation" to include all "similar-appearing lavas accumulated from several different local centers." Thus considerable confusion exists with respect to the term "Huerto" on older maps. All Huerto Andesite

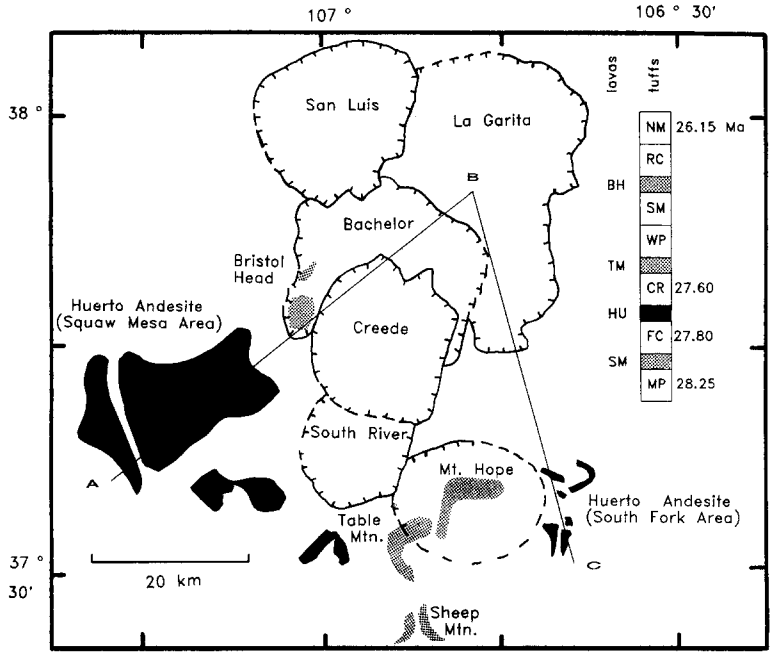

Fig. 1. Outcrop area of the Squaw Mesa and South Fork areas of the Huerto Andesite (*black*) and other andesitic lavas (*stippled*) interlayered with ash-flow tuffs. Calderas of the nearly contemporaneous ash-flow tuffs are shown, and associated tuffs are listed in stratigraphic column (Lanphere 1988; Steven et al. 1974; Lipman 1975). Points *A, B,* and *C* define the schematic cross section of Fig. 9. Abbreviations of ash-flow tuffs are: *NM*=Nelson Mtn Tuff; *SM*=Snowshoe Mtn Tuff, *WP*=Wason Park Tuff, *MM*=Mammouth Mtn Tuff, *CR*=Carpenter Ridge Tuff, *FC*=Fish Canyon Tuff, *MP*=Masonic Park Tuff. Selected ages (Ma) are shown on stratigraphic column (Lanphere 1988)

samples discussed in this report are from stratigraphic horizons unambiguously between the Fish Canyon and Carpenter Ridge Tuffs.

The Huerto Andesite is the largest (about 200 km^3) of four andesitic units (combined volume of about 300 km^3) intercalated with the voluminous dacitic and rhyolitic ash-flow tuffs of the central part of the volcanic field (Fig. 1). The other three andesitic units, the Sheep Mountain Andesite (Larsen and Cross 1956; Lipman 1975), the volcanics of Table Mountain (Steven and Lipman 1973; Lipman 1975; Williams et al. 1989) and the andesite of Bristol Head (Steven 1967; Steven et al. 1974; Lipman and Sawyer 1988), are also defined by their stratigraphic relationships with underlying and overlying ash-flow tuffs (Fig. 1). The present outcrops of all four of the above andesitic units indicate that they erupted near or peripheral to the margins of ash-flow tuff calderas (Fig. 1; Askren et al. 1988).

Ash-flow tuffs of the central San Juan volcanic field have been studied extensively, but less attention has been paid to the contemporaneous andesitic lavas. Although the eruption volume of these relatively mafic lavas is small, their presence is significant because mafic magmas may be parental to, or provide the heat sources responsible for, the generation of felsic magmas (e.g., Steven and Lipman 1976; Lipman et al. 1978; Chappell and Stevens 1988; Huppert and Sparks 1988). Therefore, we investigated the Huerto Andesite to determine the role (if any) of these andesites and related mafic magmas in the generation of the voluminous ash-flow tuffs of this classic volcanic field. Furthermore, we wanted to evaluate the magmatic processes responsible for the generation of andesitic magma far from a destructive plate tectonic margin.

Field relationships and petrography

The andesitic outcrops in both the Squaw Mesa and South Fork areas are composed of several lava flows, with flow tops and bottoms defined by highly vesicular zones. Minor amounts of breccia occur in each area. All exposures of the Huerto Andesite are porphyritic, black to brown, and contain phenocrysts (9–34%) of plagioclase (up to 20 mm)+augite (up to 2 mm)+magnetite (up to 2 mm; mostly maghemitized ± olivine (up to 2 mm; some iddingsitized ± hypersthene (up to 1 mm) ± apatite (up to 1 mm) in a fine-grained groundmass of plagioclase + pyroxene + magnetite (see Appendix for individual sample descriptions, locations, and mineral abbreviations). Olivine phenocrysts (Fo 57–68; Table 1) occur in seven samples from the Squaw Mesa area, whereas all the other phenocrysts occur in samples from both areas. The Huerto Andesite contains 20 mm, platy-plagioclase phenocrysts (Lipman 1975). Most plagioclases (An 44–80; Table 1) are euhedral, platy laths, although some rounded, embayed, and skeletal morphologies occur. Most plagioclase phenocrysts enclose patches of groundmass and exhibit fine-scale oscillatory zoning. Pyroxene phenocrysts (Table 1) are typically euhedral and unzoned. Apatite grains typically have equant morphologies and are generally attached to or included within olivine or pyroxenes. The absence of reaction rims among plagioclase, augite, magnetite, and apatite indicates that these phases co-precipitated. The large compositional range of some plagioclases record changes in magmatic temperature, pressure, or composition. We infer either olivine or hypersthene is in equilibrium with these phases, but not with each other because all but one sample (HU42) contain either olivine (or iddingsite pseudomorphs after olivine) or hypersthene, but not both. Sample HU42 contains abundant olivine with one grain of hypersthene. This single large (2 mm) grain of hypersthene (Table 1, I.D. no. 114) surrounds a small (0.1 mm) grain of olivine (Table 1, I.D. no. 113). Compositions of the hypersthene and olivine in this sample are similar to phenocryst compositions in other samples.

Using Huerto bulk compositions (Table 2) and an olivine/melt Fe-Mg distribution coefficient of 0.3 (Gill 1981), olivine in equilibrium with the Huerto magma should be Fo 62–75. This composition is similar to observed compositions (Fo 57–68; Table 1). The similarity of predicted and observed compositions, in conjunction with apparent equilibrium textures, indicates that olivine is in equilibrium (not a xenocryst or relic phase) in the Huerto Andesite.

Geochemistry

Twenty-seven samples were analyzed for whole-rock major and selected trace elements (Table 2) using a Philips PW 1410 X-ray spectrometer and XRG 3000 generator. Major elements were analyzed using glass discs fused with a flux composed of lithium tetraborate, lithium carbonate and lanthanum oxide (after Norrish and

Table 1. Representative analyses of phenocrysts in Huerto Andesite

	Olivine									Orthopyroxene						
Sample	HU42	HU42	HU42	HU42	HU47	HU47	HU47	USNM[a]		HU15	HU15	HU40	HU40	HU40	HU42	HU54
I.D. no.	113	116	117	118	22	23	24	mean	(1σ)	88	90	78	80	85	114	121
SiO_2	36.6	37.1	36.7	37.2	36.5	35.9	36.2	40.7	(0.35)	52.2	53.0	52.6	52.9	53.9	52.9	53.6
TiO_2										0.39	0.38	0.31	0.30	0.30	0.26	0.25
Al_2O_3										1.90	1.63	1.88	1.69	1.18	1.87	1.00
FeO	30.5	27.6	27.9	27.9	32.2	35.5	35.8	9.66	(0.05)	22.8	20.8	20.8	20.7	19.2	17.7	18.9
MnO	0.54	0.56	0.55	0.49	0.65	0.70	0.64	0.15	(0.03)	0.53	0.43	0.51	0.53	0.50	0.45	0.15
MgO	31.7	34.0	33.7	33.8	30.6	27.9	27.6	49.1	(0.27)	20.1	21.7	21.9	21.9	23.3	24.6	23.6
CaO										2.04	2.02	1.87	1.82	1.75	1.58	1.82
Na_2O										0.07	0.05	0.04	0.03	0.03	0.04	0.06
Total	99.34	99.26	98.85	99.39	99.95	100.0	100.24			100.03	100.02	99.98	99.88	100.16	99.4	99.38
	Fo 65	Fo 68	Fo 68	Fo 68	Fo 62	Fo 58	Fo 57			En 59	En 62	En 63	En 63	En 66	En 69	En 66

	Clinopyroxene													
Sample	HU15	HU15	HU40	HU40	HU40	HU40	HU40	HU47	HU47	HU47	HU54	HU54	USNM[a]	
I.D. no.	89	91	76	77	81	82	86	16	17	18	120	123	mean	(1s)
SiO_2	52.2	51.7	50.8	51.1	52.3	52.7	51.7	50.5	50.8	50.7	50.9	50.0	49.7	(0.17)
TiO_2	0.62	0.57	0.79	0.71	0.56	0.49	0.61	0.67	0.73	0.69	0.69	0.73	0.81	(0.02)
Al_2O_3	2.28	2.35	3.07	2.78	2.03	1.77	2.27	2.99	2.71	2.43	2.59	3.69	8.46	(0.09)
FeO	10.1	11.8	13.6	13.2	10.1	9.8	10.2	10.4	9.9	9.5	10.8	14.0	6.32	(0.08)
MnO	0.27	0.33	0.34	0.37	0.32	0.29	0.29	0.27	0.25	0.29	0.28	0.36	0.15	(0.03)
MgO	14.8	14.7	13.0	13.5	15.3	15.5	14.8	14.2	14.7	15.0	14.7	13.5	16.0	(0.11)
CaO	19.6	18.6	17.7	17.7	19.3	19.4	19.8	19.4	19.9	20.3	18.7	16.4	15.95	(0.09)
Na_2O	0.24	0.32	0.39	0.38	0.22	0.22	0.24	0.38	0.26	0.27	0.26	0.45	1.35	(0.07)
Total	100.11	100.37	99.69	99.74	100.13	100.17	99.91	98.81	99.25	99.18	98.92	99.13		
	En 16	En 19	En 23	En 22	En 16	En 16	En 17	En 17	En 16	En 15	En 18	En 24		

	Plagioclase												
Sample	HU7	HU7	HU7	HU15	HU15	HU15	HU17	HU17	HU42	HU42	HU42	USNM[a]	
I.D. no.	r2A	c2A	r3A	r1A	c1B	c2B	r3B	r2B	A1	A2	A3	mean	(1s)
SiO_2	56.9	56.6	52.0	53.5	53.8	53.0	54.0	52.2	47.9	50.3	47.3	51.0	(0.55)
Al_2O_3	26.4	26.4	29.3	29.4	29.6	29.9	29.6	30.8	33.0	31.3	33.4	30.7	(0.20)
CaO	9.5	9.6	13.0	11.2	11.6	13.1	11.9	13.8	16.3	14.1	16.8	13.7	(0.35)
Na_2O	5.83	5.14	4.10	4.69	4.24	4.07	4.91	3.94	2.39	3.42	2.20	3.49	(0.10)
K_2O	1.11	0.90	0.59	0.88	0.82	0.56	0.52	0.47	0.17	0.28	0.14	0.12	(0.05)
Total	99.74	98.64	98.99	99.67	100.06	100.63	100.93	101.21	99.76	99.40	99.84		
	An 44	An 48	An 62	An 54	An 57	An 62	An 56	An 64	An 78	An 68	An 80		

[a] Mean and SD (1σ) from replicate analyses of US Nat Mus minerals: San Carlos Forsterite for olivine analyses; Lake County Oregon Labradorite for plagioclase analyses; Kakanui Augite for pyroxene analyses. All analyses by D. Askren using Univ. S. Carolina Cameca SX-50 microprobe. I.D. no. is lab reference number

Hutton 1969). Selected trace elements (Ba, Rb, Sr, Y, Zr, Nb, Ni, and Cr) were analyzed using pressed-powder pellets (Potts 1987). Ten samples were analyzed for rare-earth and other trace elements (Th, Hf, Ta, Sc, and Co) using instrumental neutron activation following Jacobs et al. (1977). All samples were powdered in a hardened-steel shatter box; splits of selected samples were powdered in a tungsten-carbide ball mill for XRF analysis of Ni and Cr. Analytical precision and accuracy have been estimated from replicate analyses of U.S. Geological Survey standards (Table 2).

Silica contents range 55–59 wt%, and K_2O ranges 2.4–3.5 wt%. Hence the Huerto samples are at least as potassic as high-K andesite (Fig. 2), and some samples are more potassic than the most potassic andesites in the high-K subdivision of Gill (1981). All samples have normative quartz and hypersthene. Elemental abundances do not vary greatly, although samples from Squaw Mesa (samples HU42–HU54) are more variable and mafic than samples from South Fork (samples HU3–HU41). Olivine-bearing samples generally are more mafic than orthopyroxene-bearing samples (Fig. 2, 3). Silica correlates inversely with Fe_2O_3 (total iron), CaO, MgO, P_2O_5, TiO_2, Nb, Ta, Sm and Eu and positively with K_2O, Th, and Rb (Fig. 2, 3, 4). Abundances of Th, Ba, Zr and Hf remain nearly constant throughout the compositional range of silica.

Compared to bulk compositions, matrix compositions more accurately approximate melt compositions. We calculated matrix compositions by subtracting net-phenocryst compositions (from modes given in Appendix, typical mineral densities from Deer et al.

Table 2. Major and trace element compositions of Huerto Andesite. See appendix for sample descriptions and locations

	HU3	HU5A	HU7	HU8	HU11	HU13	HU15	HU17	HU18	HU20	HU22	HU25	HU26	HU28
SiO_2	57.8	57.0	57.2	57.6	57.8	57.2	58.2	57.5	57.0	58.0	57.6	56.4	56.6	58.2
TiO_2	0.87	1.04	1.02	1.00	0.97	1.03	1.04	0.89	0.94	1.03	0.97	1.03	1.08	1.02
Al_2O_3	18.1	17.9	17.7	17.0	17.4	18.0	17.8	18.5	18.0	18.1	17.2	17.6	17.4	17.1
Fe_2O_3	6.85	7.80	7.65	8.92	8.49	7.49	8.65	6.91	8.17	7.99	8.52	8.46	8.90	8.56
MnO	0.12	0.11	0.12	0.11	0.12	0.12	0.12	0.12	0.12	0.12	0.43	0.13	0.13	0.12
MgO	1.72	1.53	1.61	1.63	1.59	1.87	1.97	1.75	1.72	1.67	1.68	1.67	1.81	1.54
CaO	6.69	5.52	5.62	5.26	5.38	5.98	5.48	5.84	5.74	5.74	5.86	6.15	6.38	5.49
Na_2O	3.29	3.87	4.11	4.21	4.19	4.45	3.80	3.52	4.29	3.29	3.48	3.09	3.83	3.33
K_2O	3.25	3.18	3.29	3.34	3.27	2.75	3.32	3.09	2.91	3.45	3.24	3.14	3.04	3.36
P_2O_5	0.44	0.40	0.57	0.42	0.39	0.54	0.39	0.32	0.33	0.41	0.39	0.51	0.50	0.39
LOI[b]	1.00	1.00	1.77	1.47	1.62	1.84	1.13	1.53	1.00	1.41	1.20	1.58	0.95	0.84
Total	100.13	99.35	100.66	100.96	101.22	101.27	101.90	99.97	100.22	101.21	100.57	99.76	100.62	99.95
Ba	864		924	822	847	883	819	796	869	885	847	829	846	822
Rb	93		101	103	102	65	100	76	86	103	92	79	71	103
Th	7.8		10.9				10.3	8.8	9.3			6.6	7.0	
Nb	16		8	22	7	19	13	18	6	11	23	18	15	19
Ta	0.78		0.92				0.77	0.56	0.60			0.72	0.80	
La	40.3		47.9				44.7	41.1	41.9			39.4	39.8	
Ce	85		102				88	73	77			81	84	
Sr	593		590	575	582	735	567	661	645	603	579	704	717	575
Sm	7.6		8.9				8.6	7.4	8.0			8.1	8.5	
Eu	1.76		1.90				1.90	1.78	1.82			2.06	2.14	
Zr	249		310	285	279	216	271	260	277	287	289	227	216	276
Hf	6.1		7.0				6.8	6.0	6.07			5.0	5.3	
Tb	0.91		1.10				1.05	0.97	1.13			0.97	1.07	
Y	20		31	41	31	33	34	37	40	37	32	44	42	42
Yb	2.9		3.6				3.4	2.8	3.3			3.4	3.5	
Lu	0.48		0.56				0.52	0.39	0.46			0.54	0.57	
Sc	14.7		17.3				16.9	14.4	15.0			17.7	18.4	
Co	14.1		13.9				18.2	14.6	14.4			16.0	16.9	
Cr	14		23	23			20	16	20			10	11	20
Ni	9		11	16			16	12	5			7	5	16

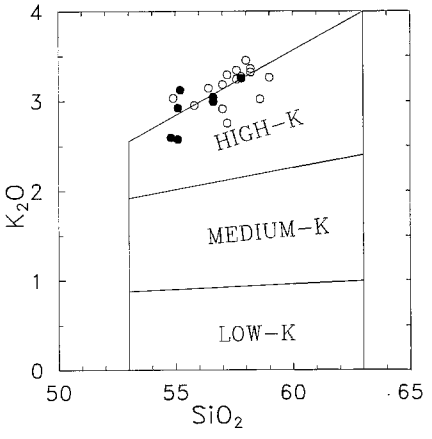

Fig. 2. Whole-rock chemical classification of the Huerto Andesite (after Gill 1981). *Filled circles* represent olivine-bearing samples; *open circles* represent orthopyroxene-bearing samples

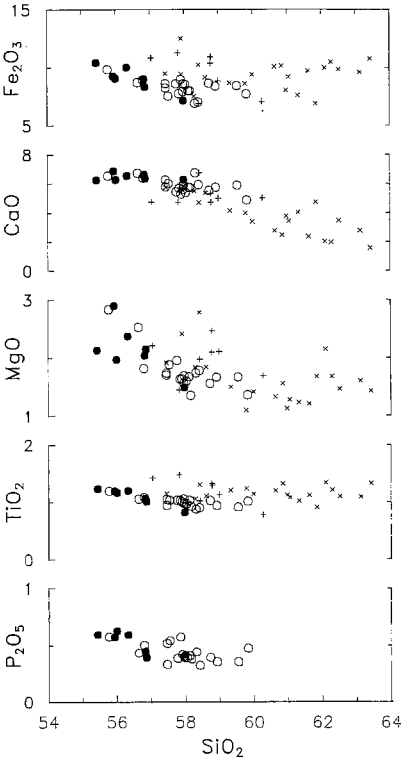

Fig. 3. Selected major elements vs SiO_2 (Fe_2O_3 = Total Fe). *Filled* and *open* circles represent whole-rock analyses of olivine- and orthopyroxene-bearing samples, respectively. *Crosses* and *Xs* represent calculated matrix compositions of olivine- and orthopyroxene-bearing samples, respectively. Estimated analytical uncertainty ($\pm 1\sigma$) for silica is 0.51 SiO_2 (Table 2); 1σ for other plotted elements is less than or equal to symbol size

Table 2 (continued)

	HU35	HU39	HU40	HU42	HU44	HU45	HU47	HU49	HU50	HU51	HU52	HU53	HU54	USGS[a]	(1σ)
SiO_2	58.1	58.1	58.6	56.6	59.0	55.2	54.8	55.8	55.1	54.9	57.3	55.7	56.4	59.0	(0.51)
TiO_2	0.93	0.93	0.90	1.01	1.00	1.15	1.18	1.19	1.18	1.22	0.81	1.04	1.05	1.02	(0.04)
Al_2O_3	18.3	17.0	16.7	19.0	17.4	17.4	16.8	16.3	16.4	17.0	19.2	17.7	18.0	17.4	(0.22)
Fe_2O_3	7.99	8.27	8.29	8.30	7.60	8.93	9.06	9.93	9.71	10.31	7.06	8.82	8.67	6.73	(0.11)
MnO	0.14	0.12	0.13	0.13	0.12	0.13	0.11	0.11	0.12	0.13	0.13	0.11	0.08	0.10	(0.02)
MgO	1.35	1.64	1.64	2.14	1.34	1.94	2.84	2.35	2.80	2.11	1.47	2.00	2.52	1.51	(0.08)
CaO	5.74	5.67	5.79	6.34	4.80	6.19	6.71	6.49	6.47	6.20	6.21	6.50	6.70	6.73	(0.11)
Na_2O	3.83	3.45	3.00	3.66	3.64	3.91	3.33	3.37	3.54	3.56	3.85	3.25	3.31	4.36	(0.50)
K_2O	3.14	3.09	3.02	2.99	3.26	3.12	2.56	2.95	2.92	3.03	2.40	2.48	2.43	2.80	(0.05)
P_2O_5	0.38	0.35	0.35	0.39	0.47	0.62	0.56	0.59	0.57	0.59	0.41	0.44	0.43	0.47	(0.02)
LOI[b]	1.03	1.25	2.01	0.23	0.33	0.23	0.89	0.94	0.56	0.65	0.40	0.54	0.54		
Total	100.93	99.87	100.43	100.79	98.96	98.82	98.84	100.02	99.37	99.70	99.24	98.58	100.13		
Ba	894		788	771	948	968	915	939		934				418	(13)
Rb	95		90	66	72	86	51	82		81				66	(3)
Th				6.8			8.6	8.4						1.2	(0.1)
Nb	17		13	14	13	21	20	28		17				14	(4)
Ta							0.98	1.30						1.3	(0.1)
La				38.9			49.9	49						16.3	(0.6)
Ce				78			100	99						38.7	(0.8)
Sr	635		645	707	563	664	639	582		529				288	(4)
Sm				7.7			10.1	10.3						6.3	(0.4)
Eu				2.07			2.22	2.14						2.11	(0.01)
Zr	264		258	193	237	268	257	260		295				228	(15)
Hf				5.13			6.94	6.85						4.6	(0.1)
Tb				0.81			1.12	0.98						0.94	(0.1)
Y	49		26	41	37	56	46	33		33				18	(2)
Yb				3.5			3.8	3.7						2.26	(0.15)
Lu				0.54			0.61	0.65						0.32	(0.02)
Sc				17.0			23.7	23.4						31.1	(0.6)
Co				58.7			73.0	29.0						36.1	(0.8)
Cr	18			17	10	14	68	59						10.9	(1.4)
Ni	12			6	3	10	33	27						12	(1)

[a] Mean and 1σ for replicate analyses of USGS standards: AGV-1 for major elements and Rb, Nb, Zr, Y; SY-3 for Ba, Sr, Ni; BCR-1 for Sc, Cr, Co; BHVO-1 for La, Ce, Sm, Eu, Tb, Yb, Lu, Th, Hf, Ta

[b] LOI = loss on ignition

Space means not analysed

1966, and representative phenocryst compositions cited in footnote of Table 3) from bulk compositions (Table 2). Calculated-silica contents (56–63 wt%) of the matrix (Fig. 3) are generally greater than bulk-SiO_2 contents. Calculated-CaO (7–2 wt%) and -MgO (3–1 wt%) contents of the matrix are generally less than bulk-CaO and -MgO contents. These two oxides correlate inversely with SiO_2. Calculated-Fe_2O_3 and -TiO_2 contents of the matrix are generally greater than bulk-Fe_2O_3 and -TiO_2 contents (Fig. 3) and show no correlation with SiO_2. The matrix-Fe_2O_3 and -TiO_2 contents should be lower than the bulk-rock contents and should correlate inversely with SiO_2 contents of the matrix because Fe and Ti are compatible elements. However, many samples contain a continuum of magnetite grain sizes from 1 mm to less than 0.05 mm. In our calculations, we chose a size of 0.2 mm as the minimum for magnetite phenocrysts because this is the smallest size magnetite phenocryst typically seen in samples that have two unambiguous-size populations of magnetite. Gill (1981, p. 276) suggests grains as small as 0.1 mm may crystallize early because of either slower growth rates or easier nucleation relative to silicates. Thus the relatively high values of calculated matrix-Fe_2O_3 and -TiO_2 contents are probably a result of our inability to differentiate phenocrysts of magnetite from groundmass magnetite in the modal analyses.

Trace elements that are typically incompatible have abundances 10 to 300 times chondritic values. When normalized to chondrites (Fig. 5), samples have low abundances of Nb, Ta, Eu and Ti relative to elements of similar compatibility; relatively felsic samples have lower abundances of P relative to elements of similar compatibility.

Origin of geochemical variations

Andesites are frequently viewed as a part of a differentiation series from basalt to more felsic compositions (e.g., Gill 1981; Grove and Kinzler 1986). Specifically in the San Juan volcanic field (e.g., Lipman et al. 1970), andesites have been cited as ultimately mantle derivatives forming the base of magma chambers whose tops erupted as silicic ash-flow tuffs. Thus understanding processes controlling even the relatively small compositional variation of the Huerto Andesite (4 wt% SiO_2) is important in completely outlining the history of the San Juan field. In general, fractionation of phenocryst phases adequately explains major- and trace-element variations within the Huerto Andesite: for example, dominant cations of all phenocryst phases show compatible behavior (i.e., abundances of these elements decrease as silica increases), hence fractionation of plagioclase, pyroxene,

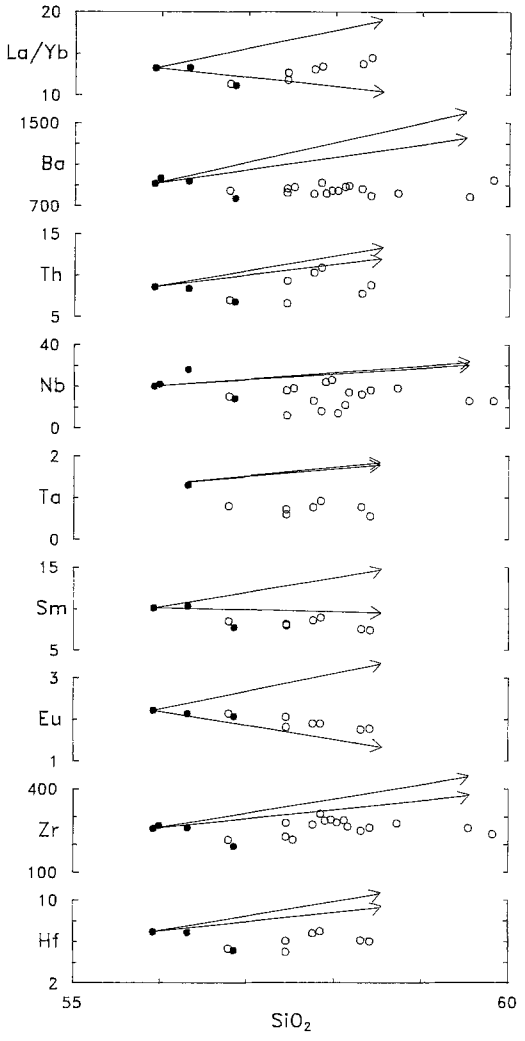

Fig. 4. Selected trace-element abundances and La/Yb ratio vs SiO_2. *Arrows* represent minimum and maximum calculated paths of simple Rayleigh crystal fractionation (Table 4). *Symbols* and *1σ* same as Fig. 3

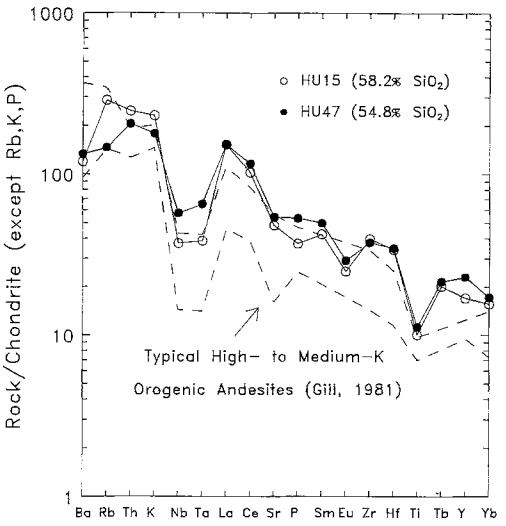

Fig. 5. Extended rare-earth element diagrams for representative samples of the Huerto Andesite. Typical orogenic andesites (from Gill, 1981) have abundances between *dashed lines*. Normalizing values (except Eu and Ba) from Thompson et al. (1984). Eu normalizing value calculated assuming Eu/Sm = 0.377 (Boynton 1984). Ba normalizing value calculated assuming Ba/La = 9.96 (Anders and Grevesse 1989)

and olivine can explain the decrease of CaO and MgO abundances with increasing SiO_2. Moreover, the observed negative Eu anomalies and decrease of Eu abundances with increasing SiO_2 are consistent with plagioclase fractionation (at the oxygen fugacites typical of andesites, Eu is divalent; Gill 1981). The fractionation of magnetite is evidenced by compatible behavior of bulk Fe_2O_3 and TiO_2 and relative depletion of Ti (Figs. 3, 5). Apatite fractionation is evidenced by compatible behavior of P_2O_5 and small relative P depletions in the most silicic samples (Fig. 3, 5). To investigate if elemental abundances can be accounted for by accumulation of crystals, we plotted modal abundances of the most abundant phenocrysts (plagioclase and clinopyroxene) against bulk concentrations of elements most compatible in these phases (Fig. 6). No positive correlations occur between these minerals and elemental abundances. Consequently, we treat the bulk compositions as magma concentrations in the following:

We modeled crystal fractionation from the most mafic sample (HU47) to yield the most felsic sample (HU44)

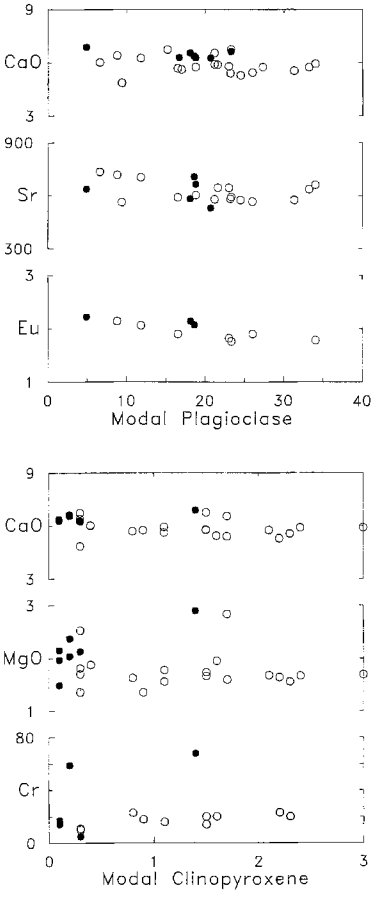

Fig. 6. Modal abundances of plagioclase and clinopyroxene vs. whole-rock abundance of elements strongly partitioned into these minerals

Table 3. Major element model using XLFRAC (Stormer and Nicholls 1978)

	Observed difference (HU44-HU47	Calculated difference (XLFRAC model)	Observed – calculated	Phase[a]	Wt% removed
Olivine model					
SiO_2	3.82	3.78	0.04	Ol (Fo 62)	3.6
TiO_2	−0.19	0.00	−0.19		
Al_2O_3	0.47	0.44	0.03	Cpx (En 43)	6.0
Fe_2O_3	−0.22	−0.38	0.16		
FeO	−1.22	−1.15	−0.06	Pl (An 62)	12.3
MnO	0.01	−0.01	0.02		
MgO	−1.55	−1.65	0.09	Mt (Usp 35)	1.8
CaO	−2.00	−1.98	−0.03		
Na_2O	0.29	0.39	−0.11	Ap	0.7
K_2O	0.69	0.74	−0.57		
P_2O_5	−0.10	−0.19	0.09	Total	24.4
		Sum of squares =	0.10		
Orthopyroxene model					
SiO_2	3.82	3.73	0.10	Opx (En 62)	6.3
TiO_2	−0.19	−0.02	−0.17		
Al_2O_3	0.47	0.44	0.03	Cpx (En 43)	4.6
Fe_2O_3	−0.22	−0.47	0.25		
FeO	−1.22	−1.10	−0.11	Pl (An 62)	14.3
MnO	0.01	0.00	0.01		
MgO	−1.55	−1.66	0.10	Mt (Usp 35)	2.2
CaO	−2.00	−1.98	−0.02		
Na_2O	0.29	0.46	−0.17	Ap	0.9
K_2O	0.69	0.86	−0.17		
P_2O_5	−0.10	−0.24	0.14	Total	28.3
		Sum of squares =	0.20		

[a] Phase compositions from Tables 1: *Ol* (HU47, I.D. no. 22); *Opx* (HU15, I.D. no. 90); *Pl* (HU15, I.D. no. c2B); *Cpx* (HU15, I.D. no. 89). *Mt* (HU15; 11.4 wt% TiO_2, 4.9 wt% Al_2O_3, 42.7 wt% Fe_2O_3, 37.1 wt% FeO). Ap (Deer et al. 1966, Table 50)

Table 4. Trace element abundances modeled by simple Rayleigh crystal fractionation

Element	Solid/melt distribution coefficients (min. & max.)	Mafic end member (HU47)	Felsic end member (HU15)	Felsic end member member (calculated min. & max.)
SiO_2		54.8	58.2	59.0
Ba	0.03–0.25	915	815	1138–1262
Rb	0.01–0.11	51	100	65–71
Th	0.01–0.16	8.6	10.3	11–12
Nb	0.17–0.23	20	13	25–26
Ta	0.17–0.23	0.98	0.77	1.6–1.7
La	0.14–0.60	49.9	44.7	56–66
Ce	0.14–0.63	99.7	87.9	111–133
Sr	0.69–1.70	639	567	522–706
Sm	0.17–1.15	10.1	8.6	8–14
Eu	0.09–1.99	2.22	1.9	1.6–3.0
Zr	0.05–0.27	257	271	317–352
Hf	0.05–0.27	6.94	6.8	8.5–9.5
Tb	0.17–1.11	1.12	1.05	1.0–1.5
Y	0.10–0.95	46	34	47–61
Yb	0.10–0.95	3.77	3.43	3.8–5.0
Lu	0.10–0.88	0.61	0.52	0.6–0.8
Sc	0.7–4.7	24	17	7–25
Co	1.4–7	73	18	10–65
Cr	3.3–86	68	20	1–32
Ni	2.0–13	33	16	1–23

Solid/melt bulk distribution coefficients have been calculated using phase proportions and mineral/melt distribution coefficients. Minimum and maximum solid/melt bulk distribution coefficients listed here are lowest and highest values calculated using the range of reported mineral/melt distribution coefficients from the literature (see text for sources) and the range of phase proportions estimated by the major element XLFRAC models (Table 3)

using major-element whole-rock and mineral chemistries and the XLFRAC program of Stormer and Nicholls (1978). The best-fit major-element model (Table 3) involves removal of 24 wt% crystals (about 12 wt% plagioclase, 6 wt% augite, 4 wt% olivine, 2 wt% magnetite, and 1 wt% apatite). Other models which yielded similar results include: (1) removal of opx instead of olivine; (2) removal of olivine and replacement of olivine by opx as differentiation proceeds. Although replacing olivine by opx as differentiation proceeds probably reflects the crystallization sequence more accurately, the resulting major-element fit was not significantly different; for simplicity, we therefore have adopted the two extreme models involving either olivine or opx (Table 3) for subsequent trace-element modeling.

Simple Rayleigh crystal fractionation has been modeled for trace-element abundances (Table 4). Bulk-distribution coefficients (D) were calculated using phenocryst proportions generated from the major-element model (Table 3) along with published mineral/melt distribution coefficients (K_D; Gill 1981; Watson and Green 1981; Green and Pearson 1987). Trace-element abundances were calcualted for a magma generated by fractional crystallization from the most mafic sample (HU47; Table 4) according to: $C_e = C_o \times F^{(D-1)}$ where C_e is concentration in the evolved magma, C_o is the concentration in the parent (here, the concentration in HU47), and F is the proportion of original liquid remaining (Cox et al. 1979).

The predicted abundances have been compared to observed trends on selected plots of trace elements vs SiO_2. Our trace-element model predicts that La/Yb ratios (Fig. 4) should remain nearly unchanged during evolution by 25 wt% fractional crystallization (Table 4); these predicted abundances closely match observed trends (Fig. 4). The lack of incompatible behavior of the REE (e.g., Sm in Fig. 4) may be explained by fractionation of small amounts of apatite (because $D_{Sm} \leq 1.15$; Table 4). Predicted abundances of typically compatible trace elements (Sc, Co, Cr, Ni) are close to observed abundances (Table 4), and the general decrease in the abundance of these elements with increasing SiO_2 substantiate the crystal-fractionation model. The REE and Sr abundances are nearly constant throughout the

Huerto Andesite as predicted by the model, with the exception of La and Ce which are slightly lower in the more felsic Huerto samples than the model predicts.

In contrast to the agreement between modeled and observed abundances of the above elements, some highly to moderately incompatible trace elements (Rb, Ba, Ta, Nb, Zr, Hf) do not behave in a manner consistent with the trace-element model. Observed abundances of Nb and Ta decrease, but the model predicts highly incompatible behavior. Observed abundances of Ba, Zr, and Hf are nearly constant, but the model predicts moderately incompatible behavior.

The disagreements between observed and modeled abundances could be explained by fractionation of phases that concentrate Zr, Hf, Ba, Th, Nb, and Ta. Zircon concentrates Zr and Hf, but according to the zircon-solubility model of Watson and Harrison (1983), magmas similar to the Huerto Andesite in bulk composition and crystallization temperature (see next section) require at least 3,000 ppm Zr to be saturated with zircon. Given the Zr content of the Huerto Andesite (up to 310 ppm), early saturation of zircon probably did not occur. Local saturation of other accessory phases has been proposed as a controlling mechanism of trace-element abundances in rhyolitic rocks (e.g., monazite, xenotime, chevkinite, allanite; Bacon 1989; Michael 1988). Failure to observe these phases or zircon with either optical microscope or electron microprobe, combined with the relatively mafic composition of the Huerto Andesite, argues against the presence of these accessory phases as fractionating phases.

Contamination by crustal material has been advocated to explain trace-element abundances of earlier (Conejos Formation) intermediate magmas in the San Juan field (Colucci et al. 1988). The abundances of several highly incompatible elements that cannot be explained by crystal fractionation (or accumulation) suggests that crustal contamination may explain some aspects of trace-element behavior; quantiative modeling awaits the result of isotopic work currently in progress.

Compared to calcalkaline andesites typical of orogenic environments (Gill 1981), the Huerto Andesite is enriched in most incompatible elements, but trace-element ratios are similar (Fig. 4). For example, the Huerto Andesite is more potassic than typical orogenic andesites and contains more La and Yb, but La/Yb values for both are 11–14 (Fig. 4). The relatively high La/Nb ratios of the Huerto Andesite reflect relative Nb-Ta depletions similar to those of destructive-margin magmas (Briqueu et al. 1984) and are rather remarkable in view of the great distance (>1,500 km) of the Huerto eruptive centers from the Oligocene subduction zone (Lipman et al. 1971; Baldridge and Olsen 1989).

Estimated temperature and pressure of equilibrium

Two-pyroxene geothermometry (Lindsley 1983) has been used to estimate magmatic temperatures. Coexisting pyroxene compositions (Table 1) are consistent with equilibrium temperatures of 1,050 to 1,070° C.

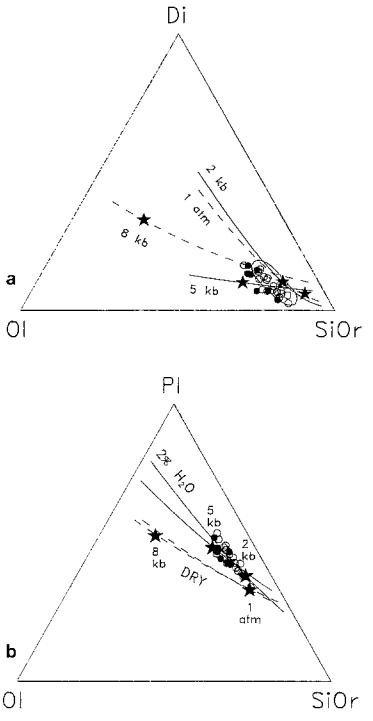

Fig. 7a, b. Projection of Huerto bulk compositions onto pseudoternary diagrams of Baker (1987). *Filled circles* represent olivine-bearing samples; *open circles* represent opx-bearing samples. 1 atm and 8 kbar cotectics (*dashed lines*) are dry; 2 and 5 kbar cotectics (*solid lines*) are 2 wt% H_2O. **a** Projection of liquid lines of multiple saturation (LLMS) on plagioclase- and magnetite-saturated diagram is used to estimate magmatic pressure. The positions of experimentally determined olivine-opx peritectics are shown as *large stars*. Calculated matrix compositions plot in *circled field*. See text for discussion. **b** Projection of LLMS on diopside- and magnetite-saturated diagram indicate ≥2 wt% H_2O in Huerto Andesite

Pressures and H_2O contents can be estimated using modal mineralogies and the position of whole-rock compositions relative to liquid lines of multiple saturation (LLMS) on pseudoternary diagrams (Baker and Eggler 1983, 1987). Huerto bulk compositions plot near isobaric LLMS in the plagioclase- and magnetite-saturated pseudoternary system olivine+diopside+[silica+orthoclase] (Fig. 7a). The bulk compositions of samples of the Huerto Andesite form an elongate field approximately parallel to the LLMS near the 2 and 5 kbar wet olivine-opx-melt peritectics. The presence of olivine in the more mafic Huerto Andesite samples shows that magmatic pressures were less than 8 kbar because at this pressure, magmas with bulk compositions similar to these olivine-bearing andesites would contain opx and no olivine (Fig. 7a). Similarly, pressures must have been greater than 1 atm because magmas similar in composition to the opx-bearing Huerto Andesite samples would contain olivine and no opx given the position of the 1-atm dry peritectic (Fig. 7a). Most olivine-bearing samples plot up-temperature of the 2 kbar peritectic, and most opx-bearing samples plot down-temperature of the 5 kbar peritectic. These mineralogic and compositional relationships suggest that the andesite equilibrated at pressures of about 2–5 kbar. Moreover, Huerto tempera-

tures estimated from the two-pyroxene geothermometer (1,050–1,070° C) are consistent with the experimental temperatures observed on the 2 and 5 kbar LLMS near the olivine-opx peritectics (1,020–1,060° C; Baker and Eggler 1987).

The range of calculated matrix compositions plot very close to bulk compositions (Fig. 7a); matrix compositions are slightly higher in SiOr (silicia + orthoclase) and lower in Ol than bulk compositions of the same samples. Matrix compositions may approach melt compositions more precisely than bulk compositions, but in this case the field for matrix compositions is essentially coincident with the field for bulk compositions. This inference is consistent with the lack of obvious crystal-accumulation control of bulk compositions (Fig. 6). Furthermore, the field for matrix compositions shows no features that are attributable to ambiguity in estimating abundances of magnetite phenocrysts. The calculated matrix compositions suggest the same approximate pressure of equilibration (2–5 kbar) as bulk compositions.

Huerto bulk compositions in the diopside- and magnetite-saturated pseudoternary system olivine + plagioclase + [silica + orthoclase] plot away from the dry LLMS and along the LLMS for 2 wt% H_2O. The proximity of the Huerto trend to the 2 wt% H_2O cotectics is consistent with a value close to 2 wt% H_2O (Fig. 7b).

Discussion

The eruptions forming the La Garita and Bachelor calderas occurred within 0.4 ± 0.2 Ma of each other, and the stratigraphic relations between the ash-flow tuffs erupted from these calderas (Fish Canyon and Carpenter Ridge Tuffs, respectively) and the Huerto Andesite require the eruptive centers for the andesitic lavas to have been active within this time span. Moreover, Whitney et al. (1988) argues that the Carpenter Ridge Tuff was a highly evolved magma produced by fractional crystallization of the parent magma of the older Fish Canyon Tuff. Such a close temporal relationship has led us to consider the plausibility of producing the Fish Canyon Tuff from the Huerto Andesite by crystal fractionation. We modeled fractionation of major elements from the most felsic Huerto Andesite sample (HU44) to the proposed Fish Canyon matrix compositions of Whitney and Stormer (1985) and Johnson and Rutherford (1989). Choosing the phase assemblage for a fractionation model is not obvious because the Huerto Andesite contains plagioclase, clinopyroxene, orthopyroxene, magnetite, and apatite phenocrysts, whereas the Fish Canyon tuff contains plagioclase, sanidine, biotite (Bi), hornblende (Hb), quartz, magnetite, ilmenite, sphene, apatite, and pyrrhotite phenocrysts and microphenocrysts. We have not modeled fractionation of the accessory phases because their effects on major-element compositions would be minimal. We have modeled fractionation of four assemblages: (1) Pl + Cpx + Opx + Mt (Huerto assemblage); (2) Pl + Opx Hb + Mt (this models Cpx disappearing through reaction with the liquid to form Hb, as suggested by Grove and Donnelly-Nolan, 1986, for Medicine Lake Volcano, California); (3) Pl + Cpx + Bi + Mt (this model Opx disappearing through reaction with the liquid and the appearance of Bi); (4) Pl + Hb + Bi + Mt (Fish Canyon assemblage). Phase assemblages 1 and 2 provide unreasonable results because Cpx or Hb must be added (not removed) to produce Fish Canyon compositions from the Huerto parent. Assemblages 3 and 4 provide results for major elements (Table 5, models A, B), where 51 and 60 wt% crystals were removed, respectively.

To evaluate the effects of new phases appearing during evolution (a requirement given the contrasting mineralogies of the Huerto and Fish Canyon samples), we have calculated an intermediate composition between the Huerto and the Fish Canyon by taking the intermediate value (between HU44 and the Fish Canyon matrix) of each major-element oxide. To evolve from HU44 to the intermediate composition, again assemblages 1 and 2 require Cpx or Hb to be added, and again assemblages 3 and 4 provide reasonable results. We considered only assemblage 4 to model evolution from the intermediate compositions to the Fish Canyon compositions because this is the eventual phenocryst assemblage of the Fish Canyon. This model (model C of Table 5: evolving from HU44 to an intermediate composition by fractionating assemblage 3, then evolving from the intermediate composition to the Fish Canyon by fractionating assemblage 4) yields results with a statistical fit only slightly better than completely evolving from the Huerto to the Fish Canyon with assemblage 3 or 4 (models A, B of Table 5). The statistical fit of the XLFRAC models is indicated by the sums of squares of residual oxides, which is the parameter the XLFRAC program minimizes.

Given the wide range of phases used to model fractionation from the Huerto to the Fish Canyon, it is not surprising that major-element models exist with fair statistical fits of the data. We compared trace-element abundances of the Huerto Andesite to the Fish Canyon and Carpenter Ridge Tuffs to provide an independent test of these models. Rubidium abundances of the Huerto Andesite (Fig. 8) increase with increasing silica contents, but the Fish Canyon Tuff has lower Rb abundances. Ratios of Ba/Sr in the Huerto Andesite remain nearly unchanged with changing silica, but the Fish Canyon and Carpenter Ridge Tuffs have significantly higher Ba/Sr ratios and appear to be highest in the samples with lowest silica contents. In simplest models, the trends of these trace elements do not support a comagmatic relation between the Huerto Andesite and the ash-flow tuffs; however, the trace-element and isotopic data are too limited to test adequately the major-element fractionation model.

An alternative to a comagmatic relation between the Huerto Andesite and the ash-flow tuffs is the possibility that intrusion of mafic magmas into continental crust could have caused melting to produce felsic magmas of the Fish Canyon and Carpenter Ridge Tuffs. Based on typical latent heats of formation and heat capacities of granitic material (Hon and Weill 1982), 33.5×10^{20} J would be required to produce the 3,000 km^3 Fish Can-

Table 5. Major element XLFRAC models testing evolution from Huerto Andesite to Fish Canyon Tuff

	Difference between observed and modeled oxide values											
	Model A		Model B		Model C							
Assemblage:	No. 3		No. 4		No. 3		No. 4		Fish Canyon compositions			
From:	HU44		HU44		HU44		IFC					
To:	FC		FC		IFC		FC					
FC matrix:	WS	JR	WS	JR	WS	JR	WS	JR	WS	IWS	JR	IJR
SiO_2	0.08	−0.11	0.10	−0.09	0.11	−0.03	0.05	−0.05	76.43	68.48	77.18	68.89
TiO_2	0.13	0.07	0.13	0.05	0.09	0.05	0.07	0.02		0.51	0.12	0.57
Al_2O_3	0.21	−0.05	0.40	0.12	0.11	−0.07	0.20	0.06	14.02	15.94	12.51	15.17
Fe_2O_3	1.14	1.07	1.30	1.27	0.78	0.76	0.65	0.64	0.23	1.01	0.30	1.04
FeO	−1.24	−1.48	−1.35	−1.64	−0.82	−1.02	−0.67	−0.82	0.33	2.86	0.28	2.84
MgO	0.99	0.66	0.92	0.67	0.66	0.46	0.46	0.34	0.45	0.91	0.11	0.74
CaO	−0.07	0.10	−0.35	−0.17	−0.12	0.01	−0.17	−0.09	2.34	3.63	0.60	2.76
Na_2O	−0.72	−0.51	−0.65	−0.42	−0.49	−0.36	−0.33	−0.21	2.92	3.33	2.94	3.34
K_2O	−0.51	0.25	−0.50	0.22	−0.32	0.20	−0.25	0.11	3.28	3.32	5.95	4.65
Sum of squares	4.68	4.14	5.37	5.04	2.10	2.01	1.33	1.27				
	Wt% phases removed by models											
Pl	29.3	36.7	29.5	37.0	19.0	25.2	14.7	18.4				
Cpx	4.3	6.0			2.7	4.1						
Opx												
Hb			4.5	7.3			2.2	3.4				
Bi	11.9	1.4	11.4	7.6	8.0	6.1	5.1	3.8				
Mt	5.5	5.4	5.4	5.2	3.7	3.9	2.7	2.6				

Abbreviations used are *Pl*=plagioclase, *Cpx*=clinopyroxene, *Opx*=orthopyroxene, *Hb*=Hornblende, *Bi*=biotite, *Mt*=magnetite; *FC*=Fish Canyon Tuff, *WS*=Fish Canyon matrix compostion calculated by Whitney and Stormer (1985), *JR*=Fish Canyon matrix composition calculated by Johnson and Rutherford (1989). *IWS & IRJ*=intermediate compositions calculated midway between Huerto and Fish Canyon (averaging HU44 with WS and JR, respectively); collectively referred to as *IFC*. Assemblage no. 3=Pl+Cpx+Bi+Mt. Assemblage no. 4=Pl+Hb+Bi+Mt. Mineral compositions were chosen to give best statistical fit of the data and are: Cpx, Opx and Mt same as Table 3; Pl from Table 1 (HU7 r2A); Hb and Bi from average values in Whitney and Stormer (1985)

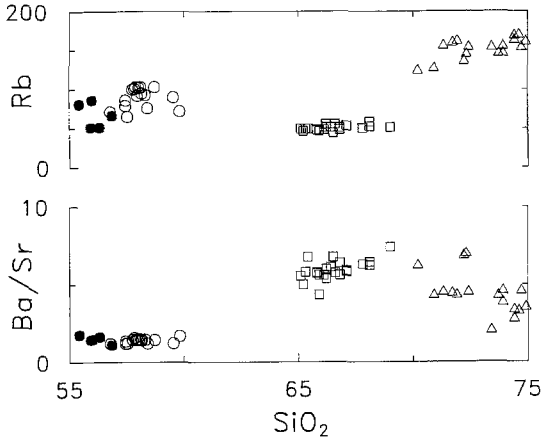

Fig. 8. Trace-element abundances vs. SiO_2 for Huerto Andesite (*filled and open circles*, as in Fig. 2), Fish Canyon Tuff (*squares*), and Carpenter Ridge Tuff (*triangles*). Fish Canyon and Carpenter Ridge data from Whitney and Stormer (1985), Whitney et al. (1988), Lipman et al. (1982)

yon Tuff (density of about 2.4; Whitney and Stormer 1985) if the crust was initially at 500° C, was heated to its solidus of approximately 650° C (assuming a heat capacity of 1.13 J/g), and melted (assuming a heat of melting of 138 J/g) and further heated to 800° C (magmatic temperature of the Fish Canyon Tuff; Whitney and Stormer 1985; assuming a heat capacity for granitic liquid of 1.38 J/g). To generate this much heat simply from crystallizing a basalt (density = 2.8, heat of crystallization = 472 J/g), 2,500 km^3 of basalt would be required to crystallize. However, fractionation of less than 400 km^3 of basalt (estimated from XLFRAC model) are required to generate observed volumes of erupted Huerto Andesite (about 200 km^3). Extending this calculation for all the ash-flow tuffs of approximately the same age (about 5,000 km^3 between 28–26 Ma) indicates that about 4,200 km^3 of mafic magma are required to provide heat for crustal melting; however less than 600 km^3 are required to produce the melting; however less than 600 km^3 are required to produce the exposed andesite (about 300 km^3) by fractional crystallization. These calculations are conservative because they assume all felsic magmas were erupted, whereas Smith (1979) estimates only about 10% of a felsic-magma chamber is erupted. Moreover, we assumed the basalts completely crystallized, but the eruption of the andesites demonstrates that their parent magmas only partially crystallized. Furthermore, the relative volume proportions of erupted andes-

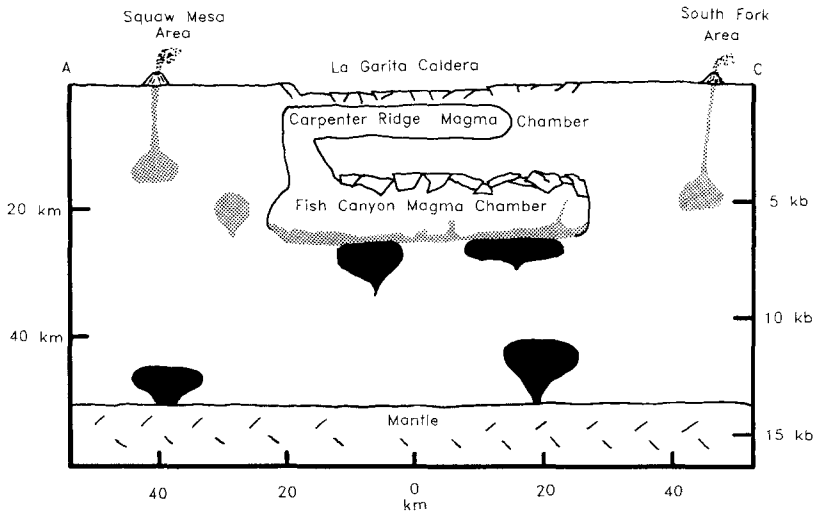

Fig. 9. Schematic model for Huerto Andesite magma chambers, with possible position of the magma chambers of the Fish Canyon and Carpenter Ridge Tuffs (see text). The diagram is along a *bent transect* through points *A*, *B*, and *C* of Fig. 1 at a time between 27.8 and 27.4 Ma. *Stippled pattern* represents andesitic magma; *black pattern* represents basaltic magma

ite and the intruded magmas of equivalent or more mafic compositions are unknown; however the inability of mafic magma to ascend through lighter crust (e.g., Cox 1980) would favor the ponding of mafic magmas in the lower crust or at the Moho. Finally, the tuffs are certainly not 100% crustal material (Lipman et al. 1978); some of the calculated volume of mafic magma may have been incorporated into the felsic magmas. As a first approximation, however, these calculations suggest that mafic plutons in the deep crust beneath the San Juan volcanic field may have been very large, perhaps as voluminous as the felsic-magma chambers associated with the region's extensive ash-flow tuffs.

Given the above, it is of interest to compare the pressure estimates of the coeval magma chambers for the Huerto Andesite and Fish Canyon-Carpenter Ridge Tuffs. The depth of the magma chamber associated with the Fish Canyon Tuff has been the subject of considerable work. Lipman et al. (1978) considered the Fish Canyon to be a "high-pressure" tuff based on the projection of its bulk composition on the albite-orthoclase-quartz system of Tuttle and Bowen (1958) and on the presence of resorbed quartz phenocrysts in a tuff with a dacitic bulk composition. Whitney and Stormer (1985) estimated a pressure of 7–9 kbar ($\pm 30\%$) based on two-feldspar and Fe-Ti oxide equilibria. Grunder and Boden (1987) used a revised Fe-Ti oxide geothermometer (Anderson and Lindsley 1985) and commented that a pressure of 9 kbar may be up to 4 kbar too high due to propagation of errors in the geothermometers. Johnson and Rutherford (1989) experimentally determined pressure to be $2–4 \pm 0.5$ kbar using the Fish Canyon phenocryst assemblage (plagioclase, sanidine, biotite, hornblende, quartz, magnetite, ilmenite, sphene, and apatite) and a melt of rhyolitic composition. Most of the disagreement concerning Fish Canyon pressure estimates stems from disagreement over the composition of the Fish Canyon melt. A melt with a high normative-anorthite content and the Fish Canyon phenocryst assemblage (Whitney and Stormer 1985) would suggest a relatively high pressure of equilibration. A melt with a low normative-anorthite content and the Fish Canyon phenocryst assemblage (Johnson and Rutherford 1989) would suggest a relatively low pressure of equilibration. The highest pressure indicated by the work of Johnson and Rutherford (1989) is 4.5 kbar; the lowest pressure indicated by Whitney and Stormer (1985; as revised by Grunder and Boden, 1987, using the revised Fe-Ti oxide geothermometer) is 4.2 kbar (i.e., 6 kbar – 30% error). These extremes overlap, and for the purpose of modeling the Huerto Andesite, we will provisionally adopt this range ($\simeq 4–5$ kbar) for the Fish Canyon Tuff.

Based on our estimates of magmatic pressures during evolution of the Huerto Andesite (2–5 kbar), pressures of equilibration in the Fish Canyon Tuff ($\simeq 4–5$ kbar), and the Carpenter Ridge Tuff (1–2 kbar, Whitney et al. 1988), and from inferred geographic locations of the eruptive centers for the Huerto Andesite (Fig. 1), we have produced a schematic cross section of the crust shown in Fig. 9. This cross section illustrates conditions just prior to the eruption of the Carpenter Ridge Tuff. The inferred mafic-magma chambers are peripheral to and beneath the likely location of the silicic-magma chamber associated with the La Garita and Bachelor calderas. As noted above, the presence of olivine phenocrysts and the relatively low silica contents in some samples of the Huerto Andesite suggest that the parent magma of the Huerto was a mantle-derived basaltic magma. The mid-crustal depths and H_2O-undersaturated conditions estimated for the Huerto Andesite are consistent with conditions suggested by Grove and Kinzler (1986) for generation of calc-alkaline andesites from olivine-normative basaltic parents. Density contrasts between such evolving mafic magmas and more felsic surrounding and overlying crustal material may have limited the ascent of these mafic magmas. In addition to supplying heat to

cause crustal melting, evolution by crystallization of basaltic magmas to less dense andesitic compositions may have allowed upward migration of magmas through depths of 15–6 km (5–2 kbar). Such magmas would erupt only where they could rise through relatively dense crust (i.e., around the margins of the Fish Canyon-Carpenter Ridge magma chamber or topographically, on the margins of the calderas). This may be manifested in the present-day by the location of Huerto Andesite outcrops peripheral to, not within, the margins of the recognized ash-flow tuff calderas. Mafic magmas rising from directly below the felsic chamber may not have penetrated beyond the base of the silicic-magma chamber because of the density contrast between mafic and felsic magmas. However, as shown in Fig. 9 the contact zone between mafic and felsic magma would likely be a zone of magma mixing: Whitney et al. (1988) report geochemical and petrographic evidence supporting magma mixing just prior to the eruption of the Carpenter Ridge Tuff, the Fish Canyon Tuff contains a few plagioclase phenocrysts with anomalously calcic cores (Whitney and Stormer 1985), and the Pb and Sr isotopic composition of the Fish Canyon indicates a significant mantle component (Lipman et al. 1978).

Conclusions

The relatively mafic character of some Huerto samples (e.g., olivine phenocrysts, low-silica contents) suggests that the Huerto Andesite was derived from a basaltic parent. Major-element and most trace-element variations can be explained by fractional crystallization of plagioclase, olivine, augite, magnetite, and apatite; olivine was probably replaced by orthopyroxene as differentiation proceeded. The most highly incompatible trace elements do not fit this simple model. Neither can fractionation of "occult" phases nor accumulation of phenocryst phases account for the observed abundances of the highly incompatible trace elements. Assimilation of crustal material may explain some of the trace-element behavior, as suggested for older units in the San Juan field by Colucci et al. (1988). Mineral and bulk compositions indicate that the Huerto Andesite last equilibrated at 1,050–1,070° C, 2–5 kbar, and $\simeq 2$ wt% H_2O. Many of the above characteristics are remarkably similar to typical orogenic andesites, thus the data we have presented are consistent with previously proposed models (e.g., Lipman et al. 1971; Engebretson et al. 1984; Baldridge and Olsen 1989) suggesting that magmatism in the San Juan field is subduction-related.

Although the andesites could be parental to the ash-flow tuffs, limited trace-element data suggest this may not be the case. Instead, mantle-derived basaltic magmas may have liberated heat while evolving to andesitic compositions, and this heat may have caused melting of the crust; subsequent melted crust, mixed with some mafic magma, may have formed felsic magma parental to the Fish Canyon and Carpenter Ridge Tuffs. Ultimately, andesitic lavas were able to erupt onto the surface, perhaps by migrating upwards around the margins of the felsic chambers; mafic magmas rising from directly below these felsic chambers may have been gravitationally trapped. Consequently, the Huerto Andesite crops out peripheral to, and not within, the calderas associated with the Fish Canyon and Carpenter Ridge Tuffs.

Acknowledgements. We thank P.W. Lipman for his assistance in understanding field relationships and for his careful review of the manuscript. We also benefited greatly from reviews by D. Wark and an anonymous reviewer. Jim Wittke's help with the Univ. S. Carolina microprobe and Tom William's help in the field are greatly appreciated. This research has been supported by NSF (EAR 8416622 to Whitney and EAR 8708307 to Roden).

Appendix

Sample locations (longitude, latitude, elevation) and descriptions:

HU3	(106°38′35″	37°35′16″	9,850 ft.)	Dark gray, hyalopilitic,		
	P1 ≤ 7 mm.	P1(23.3),	Cpx(1.5),	Opx(0.8),	Mt(1.0),	Ves(2.0)
HU5A	(106°41′25″	37°33′45″	9,670 ft.)	Gray, pilotaxitic,		
	P1 ≤ 7 mm.	P1(17.0),	Cpx(1.1),	Opx(1.8),	Mt(0.3),	Ves(10.9)
HU7	(106°41′27″	37°33′42″	9,650 ft.)	Black, hyalopilitic,		
	P1 ≤ 5 mm.	P1(16.5),	Cpx(0.8),	Opx(1.0),	Mt(0.2),	Ves(26.0)
HU8	(106°41′30″	37°33′41″	9,630 ft.)	Gray, pilotaxitic,		
	P1 ≤ 6 mm.	P1(24.5),	Cpx(2.2),	Opx(1.4),	Mt(1.0),	Ves(0)
HU11	(106°41′59″	37°33′46″	9,495 ft.)	Black, pilotaxitic,		
	P1 ≤ 7 mm.	P1(23.2).	Cpx(1.7),	Opx(1.2),	Mt(0.4),	Ves(1.8)
HU12	(106°41′14″	37°33′50″	9,370 ft.)	Brown, hyalopilitic,		
	P1 ≤ 5 mm.	P1(6.6),	Cpx(0.7),	Opx(0.4),	Mt(0.3),	Ves(5.1)
HU15	(106°41′15″	37°33′51″	9,130 ft.)	Black, pilotaxitic,		
	P1 ≤ 5 mm.	P1(26.0),	Cpx(1.6),	Opx(2.2),	Mt(0.5),	Ves(0)
HU17	(106°39′15″	37°35′36″	9,480 ft.)	Dark gray, pilotaxitic,		
	P1 ≤ 10 mm.	P1(34.0),	Cpx(1.1),	Opx(0.8),	Mt(0.2),	Ves(0.1)
HU18	(106°40′28″	37°33′07″	10,040 ft.)	Black, pilotaxitic,		
	P1 ≤ 9 mm.	P1(23.0),	Cpx(1.5),	Opx(1.6),	Mt(0.5),	Ves(2.0)
HU20	(106°41′16″	37°33′06″	9,760 ft.)	Dark gray, pilotaxitic,		
	P1 ≤ 7 mm.	P1(18.8),	Cpx(2.1),	Opx(1.6),	Mt(0.8),	Ves(6.9)

HU22	(106°41′22″	37°33′22″	9,640 ft.)	Black, pilotaxitic,		
	P1 ≤ 5 mm.	P1(21.2),	Cpx(3.0),	Opx(0.8),	Mt(0.8),	Ves(0.4)
HU25	(106°41′35″	37°33′35″	9,520 ft.)	Black, trachytic,		
	P1 ≤ 2 mm.	P1(11.8),	Cpx(0.3),	Opx(0.1),	Mt(0.4),	Ves(1.3)
HU26	(106°41′38″	37°33′35″	9,480 ft.)	Black, pilotaxitic,		
	P1 ≤ 4 mm.	P1(8.8),	Cpx(0.3),	Opx(0.1),	Mt(0.2),	Ves(0)
HU28	(106°42′10″	37°33′50″	9,400 ft.)	Black, pilotaxitic,		
	P1 ≤ 5 mm.	P1(31.3).	Cpx(2.3),	Opx(0.8),	Mt(0.8),	Ves(0)
HU35	(106°41′52″	37°30′26″	9,840 ft.)	Black, pilotaxitic,		
	P1 ≤ 6 mm.	P1(33.2),	Cpx(0.9),	Opx(0.3),	Mt(0.7),	Ves(0.2)
HU39	(106°39′46″	37°34′13″	9,560 ft.)	Gray, pilotaxitic,		
	P1 ≤ 5 mm.	P1(27.3),	Cpx(1.5),	Opx(1.0),	Mt(0.9),	Ves(0)
HU40	(106°39′30″	37°34′30″	9,480 ft.)	Gray, pilotaxitic,		
	P1 ≤ 6 mm.	P1(21.6),	Cpx(2.4),	Opx(0.6),	Mt(0.4),	Ves(0)
HU42	(107°13′20″	37°40′20″	11,760 ft.)	Black, pilotaxitic,		
	P1 ≤ 6 mm.	P1(18.6),	Cpx(0.1),	Opx(0.1),	Ol(1.0),	Mt(0.6)
	Ves(9.0)					
HU44	(107°13′30″	37°40′15″	11,760 ft.)	Black, pilotaxitic,		
	P1 ≤ 10 mm.	P1(9.4),	Cpx(0.3),	Opx(0.7),	Mt(0.5),	Ves(0)
HU45	(107°14′15″	37°40′05″	11,600 ft.)	Dark gray, pilotaxitic,		
	P1 ≤ 20 mm.	P1(18.8),	Cpx(0.1),	Ol(0.4),	Mt(0.1),	Ves(0)
HU47	(107°14′30″	37°40′00″	11,040 ft.)	Gray, pilotaxitic,		
	P1 ≤ 5 mm.	P1(4.9),	Cpx(1.4),	Ol(2.1),	Mt(1.4),	Ves(0)
HU49	(107°14′35″	37°40′00″	10,640 ft.)	Gray, pilotaxitic,		
	P1 ≤ 10 mm.	P1(18.1),	Cpx(0.2),	Ol(1.6),	Mt(0.8),	Ves(0)
HU50	(107°14′40″	37°39′55″	10,400 ft.)	Black, trachytic,		
	P1 ≤ 10 mm.	P1(21.2),	Cpx(1.7)	Opx(1.7),	Mt(1.1),	Ves(0)
HU51	(107°14′40″	37°39′50″	10,400 ft.)	Dark gray, trachytic,		
	P1 ≤ 20 mm.	P1(20.7),	Cpx(0.3),	Ol(2.3),	Mt(0.6),	ves(0.9)
HU52	(107°07′25″	37°43′15″	10,800 ft.)	Gray, pilotaxitic,		
	P1 ≤ 7 mm.	P1(16.7),	Cpx(0.1),	Ol(0.1),	Mt(0.9),	Ves(0)
HU53	(107°07′20″	37°43′10″	10,560 ft.)	Black, trachytic,		
	P1 ≤ 15 mm.	P1(23.3),	Cpx(0.2),	Ol(0.3),	Mt(0.4),	Ves(0.1)
HU54	(107°06′15″	37°44′15″	9,440 ft.)	Gray, hyalopilitic,		
	P1 ≤ 10 mm.	P1(15.2),	Cpx(0.3),	Opx(1.8),	Mt(0.3),	Ves(0)

Abbreviations used in sample descriptions: *Pl* = plagioclase, *Cpx* = clinopyroxene, *Opx* = orthopyroxene, *Ol* = olivine, *Mt* = magnetite, *Ves* = vesicles. *Numbers in parentheses* are modal %s of phenocrysts based on approximately 2,000 points per sample

References

Anders E, Grevesse N (1989) Abundances of the elements: meteoric and solar. Geochim Cosmochim Acta 53:197–214

Anderson DJ, Lindsley DH (1985) New (and final!) models for the Ti-magnetite/ilmenite geothermometer and oxygen barometer. Eos, Trans Am Geophys Union 66:416

Askren DRR (1986) Petrology and geochemistry of the Huerto Andesite, South Fork area, San Juan volcanic field, south central Colorado. Unpubl MS, Univ Georgia, Athens, Ga., USA

Askren DRR, Roden MF, Whitney JA (1988) Origin and implications of small-volume andesites interlayered with large-volume andesites of the San Juan volcanic field, south central Colorado (abstract). Geol Soc Am Abstr Program 20(7):A369

Bacon CR (1989) Crystallization of accessory phases in magmas by local saturation adjacent to phenocrysts. Geochim Cosmochim Acta 53:1055–1066

Baker DR (1987) Depths and water content of magma chambers in the Aleutian and Marianas island arcs. Geology 15:496–499

Baker DR, Eggler DH (1983) Fractionation paths of Atka (Aleutian) high-alumina basalts: constraints from phase relations. J Volcanol Geotherm Res 18:387–404

Baker DR, Eggler DH (1987) Compositions of anhydrous and hydrous melts coexisting with plagioclase, augite, and olivine or low-Ca pyroxene from 1 atm to 8 kbar – application to the Aleutian volcanic center of Atka. Am Mineral 72:12–28

Baldridge WS, Olsen KH (1989) The Rio Grande Rift. Am Sci 77:240–247

Boynton WW (1984) Cosmochemistry of the rare earth elements. In: Henderson P (ed) Rare earth geochemistry. Elsevier, Amsterdam, pp63–107

Briqueu L, Bougault H, Joron JL (1984) Quantification of Nb, Ta, Ti, and V anomalies in magmas associated with subduction zones: petrogenetic implications. Earth Planet Sci Lett 68:297–308

Chappell BW, Stevens WE (1988) Origin of infracrustal (I-type) granite magmas. In: Brown PE (ed) Origin of granites. Trans R Soc Edinburg, Earth Sci 79:71–86

Colucci MT, Ferguson KF, Balsley SD, Dungan MA, Moorbath S, Lipman PW (1988) Isotopic constraints on magma-crust interactions during the magmatic evolution of the Platoro-Summitville caldera complex, southeast San Juan volcanic field, Colorado. Geol Soc Am Abstr Program 20(7):A368

Cox KG (1980) A model for flood basalt volcanism. J Petrol 21:629–650

Cox KG, Bell JD, Pankhurst RJ (1979) The interpretation of igneous rocks. George Allen and Unwin, London

Deer WA, Howie VC, Zussman J (1966) Rock-forming minerals, vols 1–5. Longmans, Green and Co. Ltd., London

Engebretson DCA, Cox A, Thompson GA (1984) Correlation of plate motions with continental tectonics: Laramide to Basin-Range. Tectonics 3:115–119

Gill JB (1981) Orogenic andesites and plate tectonics. Springer-Verlag, Berlin Heidelberg New York

Green TH, Pearson NJ (1987) An experimental study of Nb and Ta partitioning between Ti-rich minerals and silicate liquids at high pressures and temperatures. Geochim Cosmochim Acta 51:55–62

Grove TL, Donnelly-Nolan JM (1986) The evolution of young silicic lavas at Medicine Lake Volcano, California: implications for the origin of compositional gaps in calc-alkaline series lavas. Contrib Mineral Petrol 92:281–302

Grove TL, Kinzler RJ (1986) Petrogenesis of andesites. Ann Rev Earth Planet Sci 14:417–454

Grunder AL, Boden DR (1987) Comment on '... magmatic conditions of the Fish Canyon Tuff, central San Juan volcanic field, Colorado' by Whitney and Stormer (1985) J Petrol 28:737–746

Hon R, Weill DF (1982) Heat balance of basaltic intrusion vs granitic fusion in the lower crust. Eos, Trans Am Geophys Union 63:470

Huppert HE, Sparks RSJ (1988) The generation of granitic magmas by intrusion of basalt into continental crust. J Petrol 29:599–624

Jacobs JW, Korotev RL, Blanchard DP, Haskin LA (1977) A well-tested procedure for instrumental neutron activation analysis of silicate rocks and minerals. J Radioanal Chem 40:93–114

Johnson MC, Rutherford MJ (1989) Experimentally determined conditions in the Fish Canyon Tuff, Colorado, magma chamber. J Petrol 30:711–737

Lanphere MA (1988) High-resolution $^{40}Ar/^{39}Ar$ chronology of Oligocene volcanic rocks, San Juan Mountains, Colorado. Geochim Cosmochim Acta 1425–1434

Larsen ES, Cross W (1956) Geology and petrology of the San Juan region, southwest Colorado. Am Mineral 23:227–257

Lindsley DH (1983) Pyroxene thermometry. Am Mineral 68:477–493

Lipman PW (1975) Evolution of the Platoro caldera complex and related volcanic rocks, southeastern San Juan Mountains, Colorado. US Geol Surv Prof Pap 852

Lipman PW, Steven TA, Mehnert HH (1970) Volcanic history of the San Juan Mountains, Colorado, as indicated by potassium-argon dating. Geol Soc Am Bull 81:2329–2352

Lipman PW, Prostka HJ, Christiansen RL (1971) Evolving subduction zones in the western U.S. as interpreted from igneous rocks. Science 174(4011):821–825

Lipman PW, Doe BR, Hedge CE, Steven TA (1978) Petrologic evolution of the San Juan volcanic field, southwestern Colorado: Pb and Sr isotope evidence. Geol Soc Am Bull 89:59–82

Lipman PW, Bowman HR, Knight R, Millard HT, Pallister JS, Street K, Wollenberg H, Zielinski RA (1982) Instrumental neutron activation analyses of Cenozoic volcanic rocks, phenocrysts, and associated intrusions from the southern Rocky Mountains and adjacent areas. US Geol Surv Open-File Rep 82–1069

Lipman PW, Sawyer DA (1988) Preliminary geology of the San Luis Peak quadrangle and adjacent areas, San Juan volcanic field, southwestern Colorado. US Geol Surv Open-File 88–359

Lipman PW, Steven TA (1976) Geological map of the South Fork area, eastern San Juan Mountains, southwest Colorado. US Geol Surv Misc Inv Map 1–966

Michael PJ (1988) Partition coefficients for rare earth elements in mafic minerals of high silica rhyolites: the importance of accessory mineral inclusions. Geochim Cosmochim Acta 52:275–282

Norrish K, Hutton JT (1969) An accurate X-ray spectrographic method for the analysis of a wide range of geological samples. Geochim Cosmochim Acta 33:431–453

Potts PJ (1987) A handbook of silicate rock analysis. Chapman and Hall, New York

Smith RL (1979) Ash-flow magmatism. Geol Soc Am Spec Pap 180:5–27

Steven TA (1967) Geologic map of the Bristol Head quadrangle, Colorado. US Geol Surv Map GQ-631

Steven TA, Lipman PW (1973) Geologic map of the Spar City quadrangle, Mineral County, Colorado. US Geol Surv Map GQ-1052

Steven TA, Lipman PW (1976) Calderas of the San Juan volcanic field, southwestern Colorado. US Geol Surv Prof Pap 958

Steven TA, Ratté JC (1965) Geology and structural control of ore deposition in the Creede District, San Juan Mountains, Colorado. US Geol Surv Prof Pap 487

Steven TA, Lipman PW, Hail WJ, Barker F, Luedke RG (1974) Geologic map of the Durango quadrangle, southwestern Colorado. US Geol Surv Misc Inv Map 1–764

Stormer JC, Nicholls IA (1978) XLFRAC – A program for the interactive testing of magmatic differentiation models. Comput Geosci 4:143–159

Thompson RN, Morrison MA, Hendry GL, Parry SJ (1984) An assessment of the relative roles of crust and mantle in magma genesis: an elemental approach. Philos Trans R Soc London, Ser A 310:549–590

Tuttle OF, Bowen NL (1958) Origin of granite in the light of experimental studies in the system $NaAlSi_3O_8-KAlSiO_3O_8-SiO_2-H_2O$. Geol Soc Am Mem 74

Watson EB, Green TH (1981) Apatite/liquid partition coefficients for the rare earth elements and Sr. Earth Planet Sci Lett 56:405–421

Watson EB, Harrison TM (1983) Zircon saturation revisited: temperature and composition effects in a variety of crustal magma types. Earth Planet Sci Lett 64:295–304

Whitney JA, Stormer JC (1985) Mineralogy, petrology, and magmatic conditions from the Fish Canyon Tuff, central San Juan volcanic field, Colorado. J Petrol 26:726–760

Whitney JA, Dorais MJ, Stormer JC, Kline SW, Matty DJ (1988) Magmatic conditions and development of chemical zonation in the Carpenter Ridge Tuff, central San Juan volcanic field, Colorado. Am J Sci 288A:16–44

Williams TJ, Askren DRR, Roden MF (1989) The volcanics of Table Mountain: origin and relationship to silicic volcanism, south-central San Juan volcanic field, Colorado. Eos, Trans Am Geophys Union 70(15):503

Zielinski RA, Lipman PW (1976) Trace element variations at Summer Coon volcano, San Juan Mountains, Colorado, and the origin of continental-interior andesite. Geol Soc Am Bull 87:1477–1485

Editorial responsibility: T. Grove